

This is the author's peer reviewed, accepted manuscript. However, the online version of record will be different from this version once it has been copyedited and typeset.

PLEASE CITE THIS ARTICLE AS DOI: 10.1063/1.5128717

1 **Tunable valleytronics with symmetry-retaining high polarization degree in SnS<sub>x</sub>Se<sub>1-x</sub> model**  
2 **system**

3 Shuren Lin<sup>1,2,§</sup>, Zixuan Fang<sup>1,4,§</sup>, Tingzheng Hou<sup>1,7</sup>, Ting Wan Hsu<sup>1,5</sup>, Chi H. So<sup>1</sup>, Cher Yeoh<sup>1</sup>,  
4 Roger Li<sup>1</sup>, Yin Liu<sup>1,2</sup>, Emory M. Chan<sup>2</sup>, Yu-Lun Chueh<sup>5,6</sup>, Bin Tang<sup>4</sup>, Kristin Persson<sup>1,7</sup>, Jie Yao<sup>1,3,7\*</sup>

5 <sup>1</sup> Department of Materials Science and Engineering, University of California, Berkeley, California,  
6 94720, United States

7 <sup>2</sup> The Molecular Foundry, Lawrence Berkeley National Laboratory, Berkeley, California, 94720,  
8 United States

9 <sup>3</sup> Tsinghua-Berkeley Shenzhen Institute, Shenzhen 518055, P.R.China

10 <sup>4</sup> National Engineering Research Center of Electromagnetic Radiation Control Materials, State Key  
11 Laboratory of Electronic Thin Films and Integrated Devices, University of Electronic Science and  
12 Technology of China, Chengdu 611731, P.R. China

13 <sup>5</sup> Department of Materials Science and Engineering, National Tsing Hua University, Hsinchu  
14 30013, Taiwan, Republic of China

15 <sup>6</sup> State Key Laboratory of Advanced Processing and Recycling of Non-ferrous Metals, Lanzhou  
16 University of Technology, School of Materials Science and Engineering, Lanzhou University of  
17 Technology, Lanzhou 730050, P. R. China

18 <sup>7</sup> Materials Sciences Division, Lawrence Berkeley National Laboratory, Berkeley, California, 94720,  
19 United States

20 <sup>§</sup>Both authors contributed equally to this work

21 \*Corresponding author: [yaojie@berkeley.edu](mailto:yaojie@berkeley.edu)

This is the author's peer reviewed, accepted manuscript. However, the online version of record will be different from this version once it has been copyedited and typeset.

PLEASE CITE THIS ARTICLE AS DOI: 10.1063/1.5128717

22 **Abstract**

23 SnS has recently been shown to possess unique valleytronic capability with large polarization  
24 degree, where non-degenerate valleys can be accessed using linearly polarized light, bestowed  
25 upon by the unique anisotropy and wavefunction symmetry. It is thus of utmost importance to  
26 demonstrate the extension of such effects for the IV-VI system in general, thereby elucidating the  
27 generality and tunability of such valleytronics. We show the highly tunable valleytronics via gradual  
28 compositional control of the Tin(II) Sulfo-Selenide ( $\text{SnS}_x\text{Se}_{1-x}$ ) alloy system with excellent  
29 retainment of symmetry-determined selection rules. We show the presence of both  $\Gamma\text{Y}$  and  $\Gamma\text{X}$   
30 valleys in all alloy compositions via selectivity in absorption and emission of linearly polarized light  
31 by optical reflection (R)/transmission (T) and photoluminescence (PL) measurements, and tuned  
32 the bandgaps of the valleys within a range of 1.28eV to 1.05eV and 1.48eV to 1.24eV respectively.  
33 This simultaneous tuning of non-degenerate valleys agrees well with theoretical calculations. We  
34 then fitted the bandgap values in compositional space, obtaining the bowing parameters as a  
35 useful database. We further demonstrated the feasibility of using IV-VI valleytronics systems in  
36 general by elucidating the retainment of strong polarization degrees of as high as 91% across all  
37 compositions. The generalization of such purely symmetry-dependent valleytronics also opens up  
38 opportunities for discovery of more multi-functional materials.

39

This is the author's peer reviewed, accepted manuscript. However, the online version of record will be different from this version once it has been copyedited and typeset.

PLEASE CITE THIS ARTICLE AS DOI: 10.1063/1.5128717

40 The field of valleytronics presents great opportunities in providing an additional valley degree of  
41 freedom in the control of electronic systems [1] [2]; much promise in utilizing this unique material's  
42 or system's properties hinges upon the ability to access and hence control each valley selectively.  
43 Earlier work on valleytronics demonstrated the selective population of degenerate conduction band  
44 minima, using strong biases, in systems such as Si [3] [4], AIAs [5] [6], and diamond [7]. More  
45 recently, theoretical work on graphene valleytronics [8] has led to the exploration of valleytronics in  
46 two-dimensional (2D) systems.

47 One of the most effective and well-exploited way to explore the valleys of a material is to leverage  
48 the light-matter interaction; in essence, certain polarization of light is used to selectively populate  
49 each valley, which can then form different population states where on-off information can be  
50 subsequently utilized. Previous reports of valleytronic behavior on 2D transition metal  
51 dichalcogenides (TMDCs) have demonstrated selective optical valley excitation with varying  
52 degrees of success [9] [10] [11] [12]. These reports have generated renewed interest in the  
53 valleytronics field, one of which being the actual manipulation of valley population under ambient  
54 and bias-free conditions with a high polarization degree, which was only recently reported [13],  
55 where we demonstrated a form of valleytronics in Tin(II) Sulfide (SnS).

56 Such valleytronics has a two-fold manifestation. First, the two sets of valleys in SnS reside along  
57 the  $\Gamma Y$  and  $\Gamma X$  directions in reciprocal space respectively, and, by the selection rules, are  
58 exclusively selected by y and x polarized light respectively (Supplementary Text S1, adapted from  
59 [13]). Second, the anisotropic nature of the material bestows upon the valleys the non-degeneracy  
60 in bandgap values. As such, both incident light polarization and energy can potentially be used to  
61 independently access each valley, granting the material system more flexibility in terms of  
62 excitation conditions.

63 An important extension to such flexibility is then to expand such valleytronics to the rest of the IV-  
64 VI family, which will not only allow a wider wavelength range for excitation/emission but, more  
65 importantly, prove that such valleytronics is a general behavior within the material system.

66 Herein, we report a model system in  $\text{SnS}_x\text{Se}_{1-x}$ ,  $0 \leq x \leq 1$ , demonstrating both the retainment of valley  
67 selectivity and the gradual tuning of bandgaps at both valleys across all alloy compositions. The

This is the author's peer reviewed, accepted manuscript. However, the online version of record will be different from this version once it has been copyedited and typeset.

PLEASE CITE THIS ARTICLE AS DOI: 10.1063/1.5128717

68 retainment of PL intensity and polarization degrees across the whole compositional range proves  
69 that members of the  $\text{SnS}_x\text{Se}_{1-x}$  family are suitable for such valleytronics in general.

70 We also demonstrate the continuous tuning of bandgaps for both valleys across the whole  
71 compositional range; the range of bandgaps (1.28eV to 1.05eV and 1.48eV to 1.24eV for the two  
72 valleys respectively) is much larger than that of 2D semiconductor alloys [14] [15] [16] [17],  
73 especially when considering the combined effects of both valleys under different polarizations.  
74 Furthermore, typical advantages of semiconductor alloys over pure semiconductors, including the  
75 flexibility in choice of synthesis methods [16] and the additional parameter of lattice matching [18],  
76 can be utilized on top of bandgap tunability.

77  $\text{SnS}_x\text{Se}_{1-x}$  was chosen because of the similarity in band structures for SnS and SnSe, with the  
78 presence of two valleys along the  $\Gamma Y$  and  $\Gamma X$  axes and the band separation at the  $\Gamma$  point having a  
79 larger value than the two valleys [19]. Since both materials' band structures arise from  
80 combinations of the same constituent wavefunctions [20], which satisfies the same symmetry  
81 considerations [21], valley selection rules in SnS have to also apply to SnSe, along with all  
82  $\text{SnS}_x\text{Se}_{1-x}$  compositions.

83 Both SnS and SnSe have the Pm $\bar{c}$ n crystal structure with an orthorhombic unit cell comprising of  
84 puckered layers [22], and the lattice parameters of  $\text{SnS}_x\text{Se}_{1-x}$  has been experimentally shown to  
85 vary gradually across the alloy compositions [23]. The 2x2 supercells of SnS, SnSe, and a  
86 representative  $\text{SnS}_{0.5}\text{Se}_{0.5}$  alloy are presented in Fig. 1a. Using the fitted lattice parameters from  
87 [23] and adopting the simplest case of homogeneous alloying [16], our density functional theory  
88 (DFT) calculations yield band structures with two local band gaps along the  $\Gamma Y$  and  $\Gamma X$  axes,  
89 denoted by  $E_{g,\Gamma Y}$  and  $E_{g,\Gamma X}$  respectively, across the whole compositional range (Fig. 2 and Fig. S1).

90 We synthesized  $\text{SnS}_x\text{Se}_{1-x}$  microplates,  $0 \leq x \leq 1$  in nominal increments of  $\Delta x = 0.125$  via Physical  
91 Vapor Deposition (PVD) and observed their flat morphology via SEM. Fig. 1b shows the optical  
92 microscope image, SEM image and SEM-EDX mappings of Sn, S, and Se of a representative  
93 nominally  $\text{SnS}_{0.875}\text{Se}_{0.125}$  alloy (The peak intensities for S and Se in the SEM-EDX spectra as well  
94 as images and mapping results of other alloys are presented in Fig. S2 and Fig. S3 respectively).

This is the author's peer reviewed, accepted manuscript. However, the online version of record will be different from this version once it has been copyedited and typeset.

PLEASE CITE THIS ARTICLE AS DOI: 10.1063/1.5128717

95 The exact S:Se ratios obtained from SEM-EDX follow a gradual trend and were used for  
96 quantitative analysis.

97 From the plot of actual composition versus nominal (design) composition (Fig. 1c), we can see that  
98 the Se content of all compositions is consistently higher than the design amount. This can be  
99 attributed to the lower equilibrium vapor pressure of SnSe as compared with SnS [24] [25], which is  
100 commonly reflected in the higher required PVD growth temperature of SnSe as compared with SnS  
101 [26] [27]. Our SEM-EDX results reflect the compositional tunability using our growth method.  
102 Further tuning, especially for large S content, is beyond the scope of this work, but should also be  
103 achievable using S compensation [28] or multi-sourced CVD methods [29] [30].

104 Raman spectra of SnS [26] and SnSe [27] under -z excitation (perpendicular to the layers) contain  
105 characteristic peaks that correspond to three  $A_g$  modes and one  $B_{3g}$  mode. We observed that these  
106 modes follow gradual shifts for the alloys (Fig. 1d and Fig. 1e). Note that the composition values  
107 are nominal, not actual. The larger change of actual composition from SnS to  $\text{SnS}_{0.875}\text{Se}_{0.125}$  leads  
108 to the rapid change of  $B_{3g}$  modes. We used the relative peak intensities [27] to determine the  
109 armchair ( $y$ ) and zigzag ( $x$ ) directions of each alloy composition, and presented the respective  
110 spectra under 532nm excitation when the incident polarization is aligned along the  $x$  and  $y$  axes for  
111 parallel (Fig. 1d) and cross (Fig. 1e) polarization configurations. Note that the peak for the  $A_{1g}^{(1)}$   
112 mode of SnSe cannot be observed due to the wavenumber being lower than the Raman filter  
113 edge. Also, for clarity, Raman spectra aligned along the  $y$  axis under parallel excitation is repeated  
114 using 785nm excitation to clearly distinguish and reveal the trends for the  $A_{1g}^{(3)}$  modes of the alloys  
115 (Fig. S4).

116 We observed a clear two-mode behavior for all Raman peaks, where the alloys can exhibit two  
117 peaks (SnS-like and SnSe-like) that belong to the same Raman mode. This alloy behavior can be  
118 explained using the modified random element isodisplacement (MREI) model [17] [31], where  
119 strong S-Se interactions gives two eigenvalues, one SnS-like and one SnSe-like, as the solutions  
120 to the quadratic equation of the model. This observation agrees with the common understanding  
121 that SnS and SnSe possess comparable interlayer and intralayer forces, as evidenced by the  
122 relatively small difference in interlayer and intralayer atomic distances [19]. Since all of the Raman

This is the author's peer reviewed, accepted manuscript. However, the online version of record will be different from this version once it has been copyedited and typeset.

PLEASE CITE THIS ARTICLE AS DOI: 10.1063/1.5128717

123 modes of concern here are related to relative interlayer motions [27], S-Se interactions should be  
124 significant, which explains the two-mode behavior.

125 Tunability of bandgap values at each valley is demonstrated using reflection (R) and transmission  
126 (T) as well as PL measurements, following the same protocol in our previous work on SnS [13].  
127 White light R and T measurements were conducted with the incident excitation polarized along the  
128  $y$  or  $x$  direction, hence demonstrating valley selectivity for absorption. Normalized Tauc plots are  
129 presented in Fig. 3a, clearly showing the decrease in optical bandgap values as Se content  
130 increases. Using Tauc plot analyses, we show that the bandgaps can be gradually tuned within a  
131 range of 1.28eV to 1.05eV and 1.48eV to 1.24eV for the  $\Gamma X$  and  $\Gamma Y$  valleys respectively.

132 PL measurements were conducted under parallel or cross polarization, with a second polarizer  
133 serving as an analyser placed before the detector, to further demonstrate selectivity for emission.  
134 Fig. 3b shows the PL spectra under parallel polarized 532nm excitation that is aligned to the  $y$  and  
135  $x$  axes for all alloy compositions, which elucidates the presence of a single PL peak in each  
136 spectrum that corresponds to the  $\Gamma Y$  and  $\Gamma X$  valleys respectively. (Due to the limit of the Silicon  
137 visible range detector, the PL peaks from the  $\Gamma X$  valleys cannot be detected for alloys with Se  
138 content SnS<sub>0.25</sub>Se<sub>0.75</sub> (nominal) and above. We subsequently conducted PL measurements using  
139 785nm excitation and an InGaAs infrared detector (Fig. S5) to obtain the PL peak positions of  
140 those alloys.) It can be observed that the PL peak positions red-shifts with more Se for a range of  
141 1.29eV to 1.20eV and 1.64eV to 1.45eV respectively. This agrees with the decrease in optical  
142 bandgap values obtained from R and T spectra.

143 The trends in bandgaps values for the valleys can be explained using the difference in  
144 contributions of elemental atomic orbitals to the sub-bands that make up the conduction band  
145 minimum (CBM) and valence band maximum (VBM). Orbital projected band structures in Fig. 2  
146 show that the CBMs are predominantly made up of 5p orbitals from Sn, while the VBMs are mainly  
147 composed of p orbitals of chalcogenide atoms. The contribution by Se is from the 4p orbitals,  
148 which is higher in energy as compared with the 3p orbitals of S. Therefore, with a greater Se  
149 content, the hybridised orbitals that make up the VBM of alloys will have more Se character, hence

This is the author's peer reviewed, accepted manuscript. However, the online version of record will be different from this version once it has been copyedited and typeset.

PLEASE CITE THIS ARTICLE AS DOI: 10.1063/1.5128717

150 leading to a smaller bandgap. This is clearly shown in Fig. 2b, where the VBM of  $\text{SnS}_{0.5}\text{Se}_{0.5}$  is  
 151 contributed mostly by Se orbitals.

152 The trends in bandgap values agree with the calculated band structure (Fig. 2 and Fig. S1),  
 153 ascertaining the validity of the optical measurement results. More importantly, our DFT calculations  
 154 show that the CBM and VBM along  $\Gamma X$  ( $\Gamma Y$ ) is contributed almost entirely by  $p_x$  ( $p_y$ ) orbitals. This  
 155 confirms that the symmetry of the wavefunctions that make up the CB and VB along  $\Gamma X$  and  $\Gamma Y$  for  
 156 all alloy compositions remain the same as that of  $\text{SnS}$ ; the irreducible representations of orbitals  
 157 that make up the CBM and VBM remain the same across all compositions.

158 Hence, using our previously discussed selection rules (Supplementary Text S1, adapted from [13]),  
 159 CB to VB transitions at the valleys can only occur for light polarized along the  $x$  and  $y$  directions  
 160 respectively; valley selectivity is retained across all  $\text{SnS}_x\text{Se}_{1-x}$  alloy compositions, in agreement  
 161 with the experimental results shown above.

162 We further quantify such retainment of valley selectivity with the figures of merit, the intervalley  
 163 ( $P_{\text{intervalley},\Gamma Y/\Gamma X}$ ) and intravalley ( $P_{\text{intervalley},\Gamma Y/\Gamma X}$ ) polarization degrees, as defined in our previous work  
 164 [13] as:

$$165 \quad P_{\text{intervalley},\Gamma X} = \frac{I_{\Gamma X\parallel}(\theta=90^\circ) - I_{\Gamma Y\parallel}(\theta=90^\circ)}{I_{\Gamma X\parallel}(\theta=90^\circ) + I_{\Gamma Y\parallel}(\theta=90^\circ)} \quad \text{and} \quad P_{\text{intervalley},\Gamma Y} = \frac{I_{\Gamma Y\parallel}(\theta=0^\circ) - I_{\Gamma X\parallel}(\theta=0^\circ)}{I_{\Gamma Y\parallel}(\theta=0^\circ) + I_{\Gamma X\parallel}(\theta=0^\circ)}$$

$$166 \quad P_{\text{intervalley},\Gamma X} = \frac{I_{\Gamma X\parallel}(\theta=90^\circ) - I_{\Gamma X\perp}(\theta=90^\circ)}{I_{\Gamma X\parallel}(\theta=90^\circ) + I_{\Gamma X\perp}(\theta=90^\circ)} \quad \text{and} \quad P_{\text{intervalley},\Gamma Y} = \frac{I_{\Gamma Y\parallel}(\theta=0^\circ) - I_{\Gamma Y\perp}(\theta=0^\circ)}{I_{\Gamma Y\parallel}(\theta=0^\circ) + I_{\Gamma Y\perp}(\theta=0^\circ)}$$

167 It is clear from Fig. 3b, that  $P_{\text{intervalley},\Gamma Y/\Gamma X}$  (Fig. 4a) remains significant across all compositions.  
 168 Results from PL measurements conducted under cross polarization were then used to calculate  
 169  $P_{\text{intervalley},\Gamma Y/\Gamma X}$ , which are also presented in Fig. 4a. The strong polarization degrees of, for example,  
 170 up to 91% and an average of 75% for  $P_{\text{intervalley},\Gamma X}$ , proves that the alloys still rival results obtained  
 171 using monolayer TMDCs from experiments conducted at cryogenic temperatures [9] [12] [32].

172 Our PL, white light R and T and theoretical results clearly show tunable, wavelength-dependent,  
 173 non-degenerate valleytronics in  $\text{SnS}_x\text{Se}_{1-x}$ . For practical purposes, it is thus important to apply  
 174 Vegard's law [33] to generate a database for the bandgap values and the bowing parameter,  $b$

This is the author's peer reviewed, accepted manuscript. However, the online version of record will be different from this version once it has been copyedited and typeset.

PLEASE CITE THIS ARTICLE AS DOI: 10.1063/1.5128717

175 [34]. Fig. 4b shows the optical bandgap values obtained via white light R and T as well as PL for  
176 both valleys, plotted in compositional space. Using

$$177 \quad E_{g,SnS_xSe_{1-x}} = xE_{g,SnS} + (1-x)E_{g,SnSe} + bx(1-x)$$

178 we obtained  $b_{\Gamma\gamma(\text{white light})} = -0.11185\text{eV}$ ,  $b_{\Gamma\chi(\text{white light})} = -0.0331\text{eV}$ ,  $b_{\Gamma\gamma(\text{PL})} = -0.06843\text{eV}$ , and  $b_{\Gamma\chi(\text{PL})} = -$   
179  $0.0521\text{eV}$ , respectively. The fitted functions are also overlaid in Fig. 4b. We note that the bowing  
180 parameters obtained for the valleys using both absorption and PL methods are close to each other  
181 and very small [35], which gives a rather linear relationship that simplifies the tunability. Calculated  
182 bandgaps (obtained from Fig.S1) values are also presented in the inset of Fig. 4b.

183 While beyond the scope of this work, we also observe from Fig. 3b and Fig. S5 that the full-width at  
184 half-maximum (FWHM) of the PL peaks (Fig. S6a and Fig. S6b) increases with greater Se content,  
185 along with a decrease in PL intensity (Fig. S6c). We further conducted power-dependent PL  
186 measurements, fitted, and analysed the PL peak intensity using a power law,  $I_{PL} \propto I_{excitation}^k$ , as  
187 presented in Supplementary Text S2 and Fig. S6d, to understand the effect on the nature of the  
188 bandgap transitions with alloying.

189 In conclusion, we have conducted reflection/ transmission and PL measurements that show the  
190 tunability of the two bandgaps from 1.28eV to 1.05eV and 1.48eV to 1.24eV in bulk  $SnS_xSe_{1-x}$  for  
191 the valleys residing along  $\Gamma\chi$  and  $\Gamma\gamma$  respectively. These valleys retained the selection rules as  
192 previously reported in bulk SnS, under ambient conditions and without additional biases. The  
193 valleys are strongly and solely excited by y- and x-polarized light and also mostly emit y- and x-  
194 polarized light respectively, effectively serving as a demonstration of tunability of non-degenerate  
195 valleys. Our model system also has, nominally, the advantage of superior polarization degrees of  
196 up to 91%. We also elucidate the bandgap bowing parameters for the alloy system and revealed  
197 some insights of the transitions, including quantitative analyses that revealed recombination  
198 mechanisms to be dominantly independent of dopants levels. Such discovery may allow future  
199 work on practical applications with  $SnS_xSe_{1-x}$  as a model system to be conducted.



This is the author's peer reviewed, accepted manuscript. However, the online version of record will be different from this version once it has been copyedited and typeset.

PLEASE CITE THIS ARTICLE AS DOI: 10.1063/1.5128717

## 200 References

- 201 <sup>1</sup> J.R. Schaibley, H. Yu, G. Clark, P. Rivera, J.S. Ross, K.L. Seyler, W. Yao, and X. Xu, Nat. Rev. Mater. **1**, 16055  
202 (2016).
- 203 <sup>2</sup> X. Xu, W. Yao, D. Xiao, and T.F. Heinz, Nat. Phys. **10**, 343 (2014).
- 204 <sup>3</sup> L.J. Sham, S.J. Allen, A. Kamgar, and D.C. Tsui, Phys. Rev. Lett. **40**, 472 (1978).
- 205 <sup>4</sup> K. Takashina, Y. Ono, A. Fujiwara, Y. Takahashi, and Y. Hirayama, Phys. Rev. Lett. **96**, 236801 (2006).
- 206 <sup>5</sup> Y.P. Shkolnikov, E.P. De Poortere, E. Tutuc, and M. Shayegan, Phys. Rev. Lett. **89**, 22 (2002).
- 207 <sup>6</sup> O. Gunawan, Y.P. Shkolnikov, K. Vakili, T. Gokmen, E.P. De Poortere, and M. Shayegan, Phys. Rev. Lett. **96**,  
208 186404 (2006).
- 209 <sup>7</sup> J. Isberg, M. Gabrysch, J. Hammersberg, S. Majdi, K.K. Kovi, and D.J. Twitchen, Nat. Mater. **12**, 760 (2013).
- 210 <sup>8</sup> A. Rycerz, J. Tworzydło, and C.W.J. Beenakker, Nat. Phys. **3**, 172 (2007).
- 211 <sup>9</sup> H. Zeng, J. Dai, W. Yao, D. Xiao, and X. Cui, Nat. Nanotechnol. **7**, 490 (2012).
- 212 <sup>10</sup> D. Xiao, G. Bin Liu, W. Feng, X. Xu, and W. Yao, Phys. Rev. Lett. **108**, 196802 (2012).
- 213 <sup>11</sup> W.T. Hsu, Y.L. Chen, C.H. Chen, P.S. Liu, T.H. Hou, L.J. Li, and W.H. Chang, Nat. Commun. **6**, 1 (2015).
- 214 <sup>12</sup> K.F. Mak, K. He, J. Shan, and T.F. Heinz, Nat. Nanotechnol. **7**, 494 (2012).
- 215 <sup>13</sup> S. Lin, A. Carvalho, S. Yan, R. Li, S. Kim, A. Rodin, L. Carvalho, E.M. Chan, X. Wang, A.H. Castro Neto, and J.  
216 Yao, Nat. Commun. **9**, 1455 (2018).
- 217 <sup>14</sup> Q. Feng, N. Mao, J. Wu, H. Xu, C. Wang, J. Zhang, and L. Xie, ACS Nano **9**, 7450 (2015).
- 218 <sup>15</sup> C.S. Jung, F. Shojaei, K. Park, J.Y. Oh, H.S. Im, D.M. Jang, J. Park, and H.S. Kang, ACS Nano **9**, 9585 (2015).
- 219 <sup>16</sup> S. Susarla, A. Kutana, J.A. Hachtel, V. Kochat, A. Apte, R. Vajtai, J.C. Idrobo, B.I. Yakobson, C.S. Tiwary, and  
220 P.M. Ajayan, Adv. Mater. **29**, 1702457 (2017).
- 221 <sup>17</sup> M. Zhang, J. Wu, Y. Zhu, D.O. Dumcenco, J. Hong, N. Mao, S. Deng, Y. Chen, Y. Yang, C. Jin, S.H. Chaki, Y.S.  
222 Huang, J. Zhang, and L. Xie, ACS Nano **8**, 7130 (2014).
- 223 <sup>18</sup> I. Vurgaftman, J.R. Meyer, and L.R. Ram-Mohan, J. Appl. Phys. **89**, 5815 (2001).
- 224 <sup>19</sup> L.C. Gomes and A. Carvalho, Phys. Rev. B - Condens. Matter Mater. Phys. **92**, 085406 (2015).
- 225 <sup>20</sup> L. Makinistian and E.A. Albanesi, Phys. Status Solidi Basic Res. **246**, 183 (2009).
- 226 <sup>21</sup> D.K. Ferry, in *Semicond. Bond. Bands* (IOP Publishing Ltd, Bristol, 2013).
- 227 <sup>22</sup> H.R. Chandrasekhar, R.G. Humphreys, U. Zwick, and M. Cardona, Phys. Rev. B **15**, 2177 (1977).
- 228 <sup>23</sup> T.H. Patel, R. Vaidya, and S.G. Patel, Bull. Mater. Sci. **26**, 569 (2003).
- 229 <sup>24</sup> V. Piacente, S. Foglia, and P. Scardala, J. Alloys Compd. **177**, 17 (1991).
- 230 <sup>25</sup> F. Zocchi and V. Piacente, J. Mater. Sci. Lett. **14**, 235 (1995).
- 231 <sup>26</sup> J. Xia, X.Z. Li, X. Huang, N. Mao, D.D. Zhu, L. Wang, H. Xu, and X.M. Meng, Nanoscale **8**, 2063 (2016).
- 232 <sup>27</sup> X. Xu, Q. Song, H. Wang, P. Li, K. Zhang, Y. Wang, K. Yuan, Z. Yang, Y. Ye, and L. Dai, ACS Appl. Mater.  
233 Interfaces **9**, 12601 (2017).
- 234 <sup>28</sup> Q. Li, A. Wei, J. Lu, L. Tao, Y. Yang, D. Luo, J. Liu, Y. Xiao, Y. Zhao, and J. Li, Adv. Electron. Mater. **4**,  
235 1800154 (2018).

This is the author's peer reviewed, accepted manuscript. However, the online version of record will be different from this version once it has been copyedited and typeset.

PLEASE CITE THIS ARTICLE AS DOI: 10.1063/1.5128717

- 236 <sup>29</sup> J.H. Ahn, M.J. Lee, H. Heo, J.H. Sung, K. Kim, H. Hwang, and M.H. Jo, *Nano Lett.* **15**, 3703 (2015).
- 237 <sup>30</sup> Z. Mutlu, W. Ryan J., D. Wickramaratne, S. Shahrezaei, C. Liu, S. Temiz, A. Patalano, M. Ozkan, R.K. Lake,  
238 K.A. Mkhoyan, and C.S. Ozkan, *Small* **12**, 2998 (2016).
- 239 <sup>31</sup> Y. Chen, D.O. Dumcenco, Y. Zhu, X. Zhang, N. Mao, Q. Feng, M. Zhang, J. Zhang, P.H. Tan, Y.S. Huang, and  
240 L. Xie, *Nanoscale* **6**, 2833 (2014).
- 241 <sup>32</sup> B. Zhu, H. Zeng, J. Dai, Z. Gong, and X. Cui, *Proc. Natl. Acad. Sci.* **11**, 11606 (2014).
- 242 <sup>33</sup> L. Vegard, *Zeitschrift Für Phys.* **17**, 5 (1921).
- 243 <sup>34</sup> R.E. Nahory, M.A. Pollack, W.D. Johnston, and R.L. Barns, *Appl. Phys. Lett.* **33**, 659 (1978).
- 244 <sup>35</sup> S. Adachi, in *Springer Handb. Electron. Photonic Mater.* (Springer International Publishing, Switzerland,  
245 2017), p. 733.

This is the author's peer reviewed, accepted manuscript. However, the online version of record will be different from this version once it has been copyedited and typeset.

PLEASE CITE THIS ARTICLE AS DOI: 10.1063/1.5128717

246 **Supplementary material**

247 See supplementary material for power law analyses of CB to VB transitions, which further explains  
248 bandgap transitions, as well as supporting SEM, Raman, and DFT evidences.

249 **Acknowledgements**

250 This work is supported by the Tsinghua-Berkeley Shenzhen Institute (TBSI).

251 Work at the Molecular Foundry was supported by the Office of Science, Office of Basic Energy  
252 Sciences, of the U.S. Department of Energy under Contract No. DE-AC02-05CH11231.

253 **Author contributions**

254 J.Y. coordinated the work. S.L and J.Y designed the experiments. S.L. conducted the optical  
255 measurements and analysed the data. T.W.H. and E.M.C. conducted the optical measurements.  
256 T.H. and K.P. carried out the DFT calculations and electric dipole analysis. Z.F., C.H.S., C.Y., R.L,  
257 and Y.L. synthesized and characterized the materials. S.L and J.Y wrote the manuscript with the  
258 help from all authors.

259 **Competing financial interests**

260 The authors declare no competing financial interests.

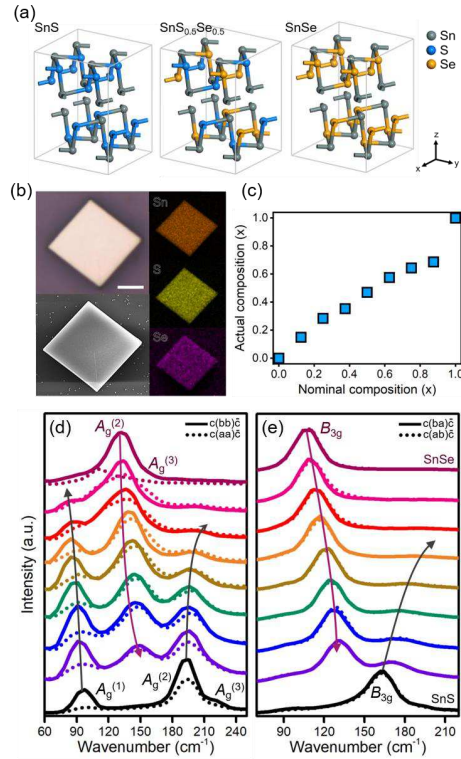
261 **Materials & Correspondence**

262 Correspondence and material requests should be addressed to Jie Yao.

This is the author's peer reviewed, accepted manuscript. However, the online version of record will be different from this version once it has been copyedited and typeset.

PLEASE CITE THIS ARTICLE AS DOI: 10.1063/1.5128717

263 **Figures**



264

265 **Fig 1: Structure and characterization of  $\text{SnS}_x\text{Se}_{1-x}$ .** (a)  $2 \times 2$  supercells of molecular structures of  
 266 SnS, SnSe, and a representative  $\text{SnS}_{0.5}\text{Se}_{0.5}$  alloy with the simplest case of homogeneous alloying.  
 267 The puckered arrangement of atoms and the high anisotropy along the  $y$  (armchair) and  $x$  (zigzag)  
 268 directions is maintained across the whole compositional range while the lattice parameters increase  
 269 with Se content. (b) Optical microscopy image, scanning electron microscopy (SEM) images and  
 270 Energy-dispersive X-ray spectroscopy (EDX) maps of a representative, nominally  $\text{SnS}_{0.875}\text{Se}_{0.125}$   
 271 sample, demonstrating a flat surface and homogeneous distribution of Sn, S, and Se. Scale bar is  
 272  $5\mu\text{m}$ . (c) Trend in actual composition versus nominal (design) composition, showing a general  
 273 excess of Se content. (d) Reflection mode,  $c(xx)\bar{c}$ , Raman spectra obtained under parallel  
 274 polarization. The first and second letters in the parentheses denotes the alignment of the incident  
 275 light and emitted signal. Only spectra aligned along  $x$  and  $y$  directions are presented, showing clear  
 276 trends in intensities for the  $A_g$  modes, thus ascertaining the identity and orientation of the measured

This is the author's peer reviewed, accepted manuscript. However, the online version of record will be different from this version once it has been copyedited and typeset.

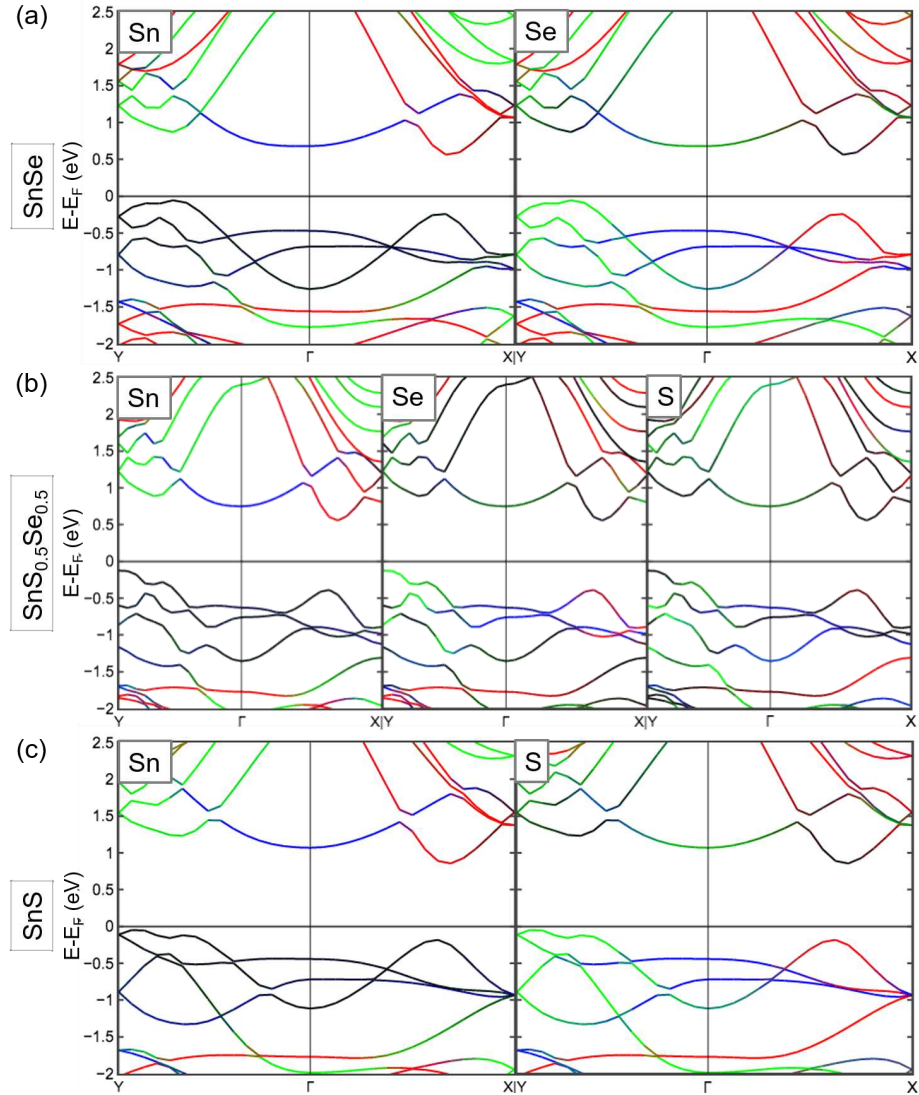
PLEASE CITE THIS ARTICLE AS DOI: 10.1063/1.5128717

- 277 samples. (e) Raman spectra obtained under cross polarization, showing clear trends in intensities  
278 for the  $B_{3g}$  modes.

This is the author's peer reviewed, accepted manuscript. However, the online version of record will be different from this version once it has been copyedited and typeset.

PLEASE CITE THIS ARTICLE AS DOI: 10.1063/1.5128717

279



280

281 **Fig 2: Calculated band structures for selected  $\text{SnS}_x\text{Se}_{1-x}$ .** Orbital projected band structures along  
 282  $Y-\Gamma-X$  and DOS of representative alloy compositions of (a) SnSe, (b)  $\text{SnS}_{0.5}\text{Se}_{0.5}$ , and (c) SnS are  
 283 presented. Band structures are projected on elements of Sn, S and Se, and  $p_x$ ,  $p_y$  and  $p_z$  orbitals.  
 284 Our elemental and orbital specific band structures denote that for all alloy compositions, p orbitals  
 285 from Sn and the chalcogenides make up predominantly the conduction and valence bands.

14

This is the author's peer reviewed, accepted manuscript. However, the online version of record will be different from this version once it has been copyedited and typeset.

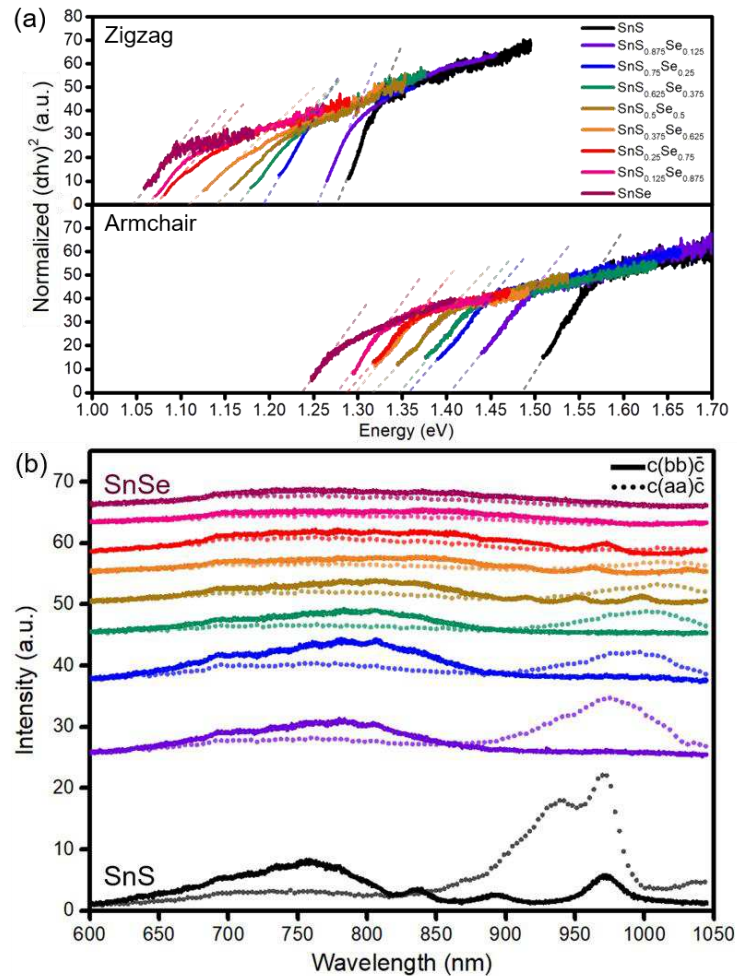
PLEASE CITE THIS ARTICLE AS DOI: 10.1063/1.5128717

286 respectively. Red, green, and blue shades correspond to contributions of each subband by  $p_x$ ,  $p_y$ ,  
287 and  $p_z$  orbitals respectively; this demonstrates that  $\Gamma X$  and  $\Gamma Y$  valleys are predominantly made up of  
288  $p_x$  and  $p_y$  orbitals respectively for all alloy compositions.

This is the author's peer reviewed, accepted manuscript. However, the online version of record will be different from this version once it has been copyedited and typeset.

PLEASE CITE THIS ARTICLE AS DOI: 10.1063/1.5128717

289



290

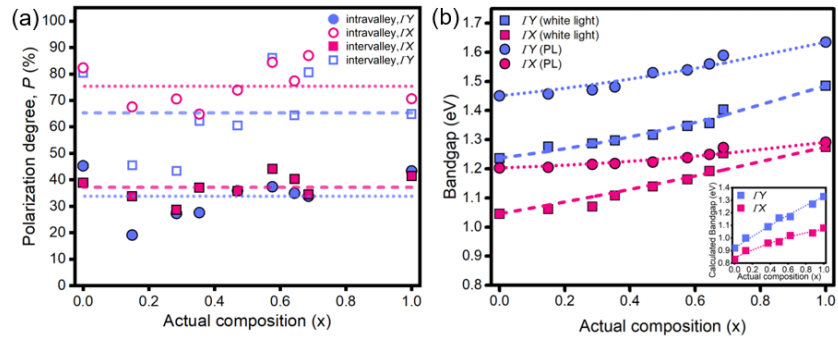
291 **Fig 3: Optical measurements of SnS<sub>x</sub>Se<sub>1-x</sub>.** (a) Normalized Tauc plots of both directions for  
 292 different alloy compositions obtained from white light R and T measurements, showing a distinct  
 293 decrease in bandgap value with increasing Se content. (b) PL peaks under parallel polarization. Only  
 294 spectra aligned along x and y directions are presented, showing that for all alloy compositions, the  
 295 high (low) energy peak has the strongest intensity when the excitation light is polarized along the y  
 296 (x) direction, showing the retainment of valley selectivity across all alloy compositions. There is also  
 297 a clear trend of decrease in bandgap value with increasing Se content.

16



This is the author's peer reviewed, accepted manuscript. However, the online version of record will be different from this version once it has been copyedited and typeset.

PLEASE CITE THIS ARTICLE AS DOI: 10.1063/1.5128717

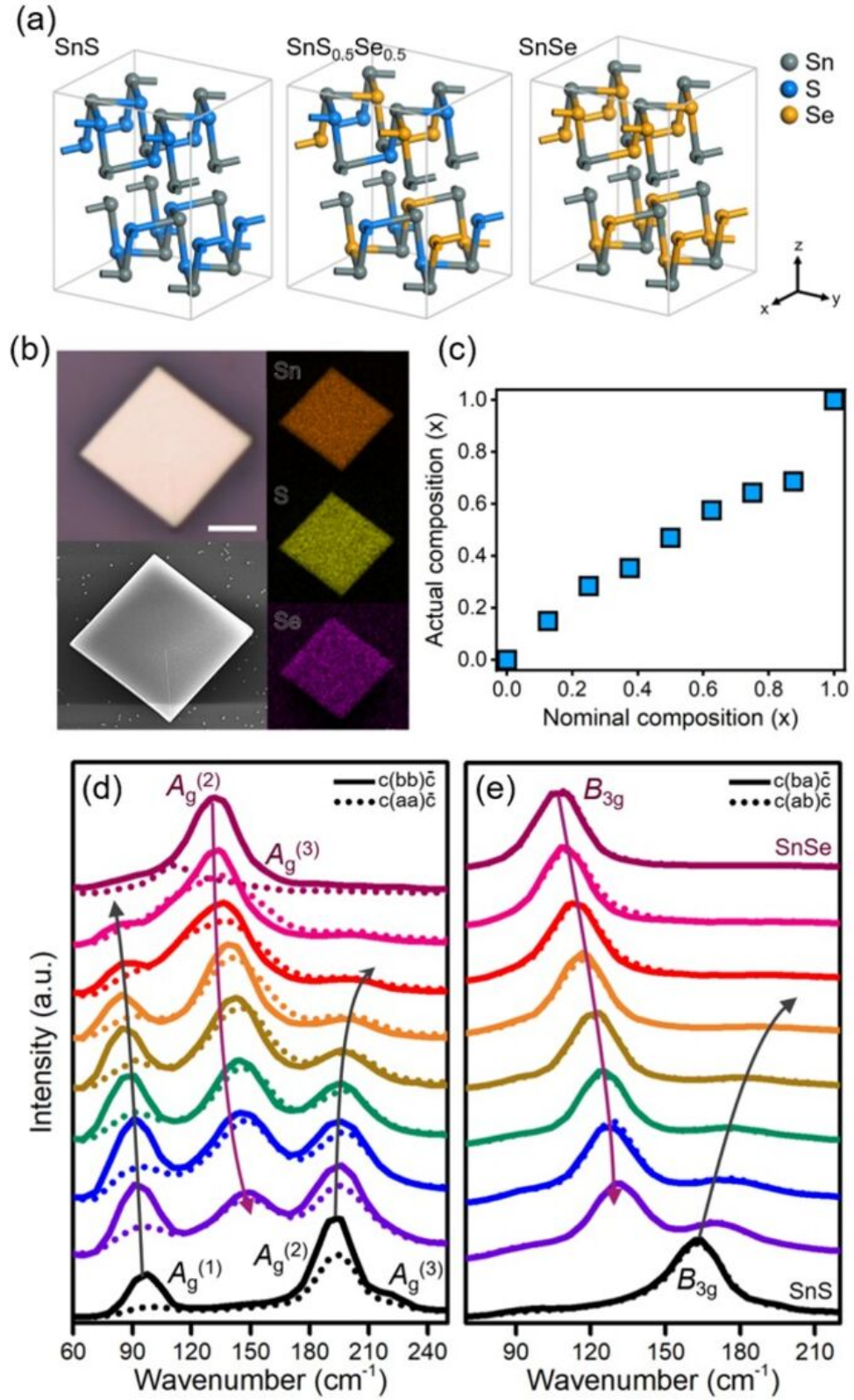


298

299 **Fig 4: Valley selectivity in SnS<sub>x</sub>Se<sub>1-x</sub>.** (a) Trends in polarization degrees with compositional  
 300 variation, showing the retainment of high valley selectivity across all alloy compositions in SnS<sub>x</sub>Se<sub>1-x</sub>.  
 301 Intervalley (intravalley) polarization degrees are presented as squares (circles), with dashed  
 302 (dotted) lines demarcating the respective average values. Solid and open data points denotes the  
 303 polarization degrees that depends predominantly on PL signals of the  $\Gamma$ Y and  $\Gamma$ X valleys respectively.  
 304 (b) Optical bandgaps obtained by white light R and T as well as PL measurements, plotted with fitting  
 305 functions using Vegard's law. Calculated bandgap values are presented in the inset, showing a  
 306 smooth variation and similar trends for both  $\Gamma$ Y and  $\Gamma$ X valleys respectively.

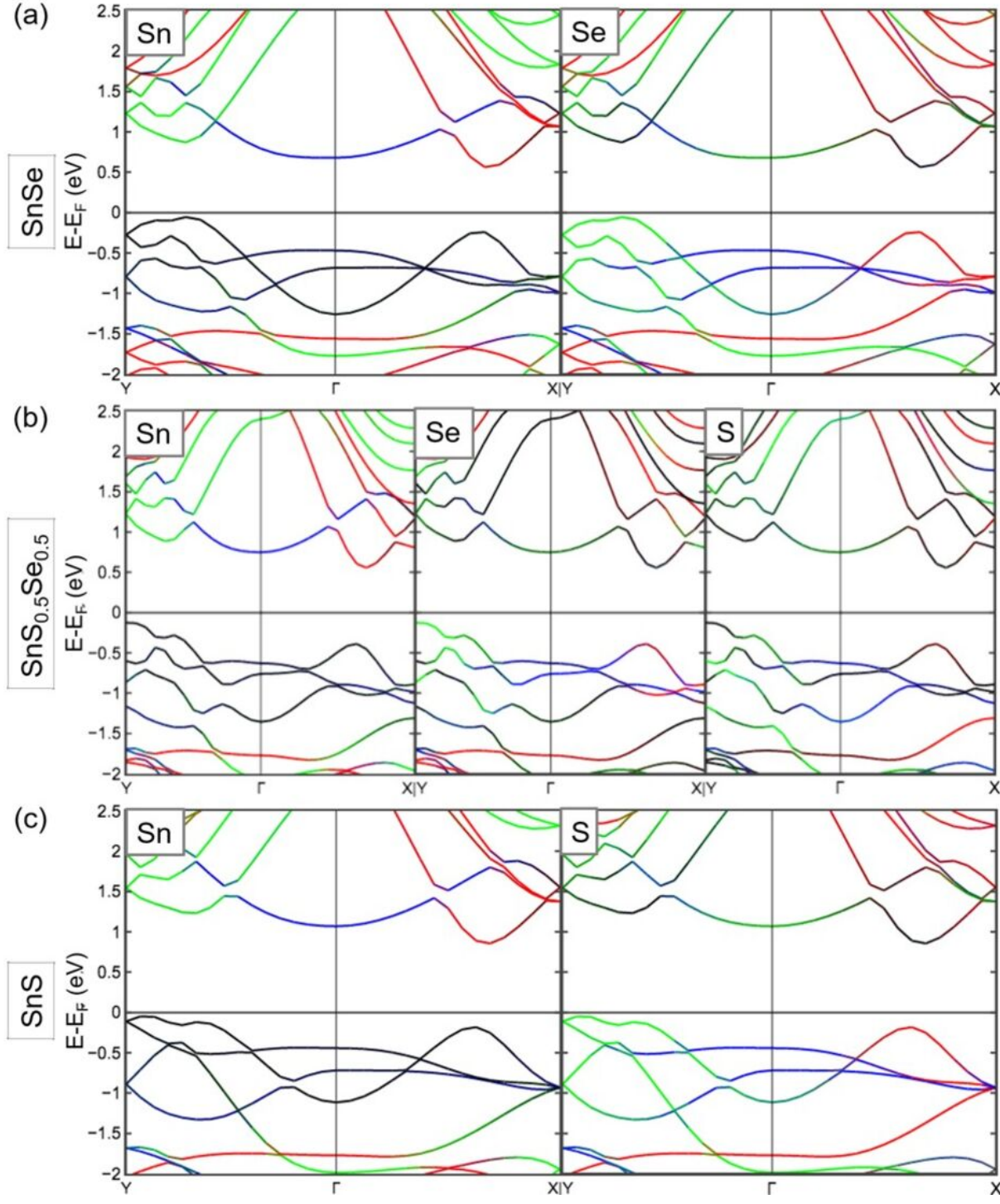
This is the author's peer reviewed, accepted manuscript. However, the online version of record will be different from this version once it has been copyedited and typeset.

PLEASE CITE THIS ARTICLE AS DOI: 10.1063/1.5128717

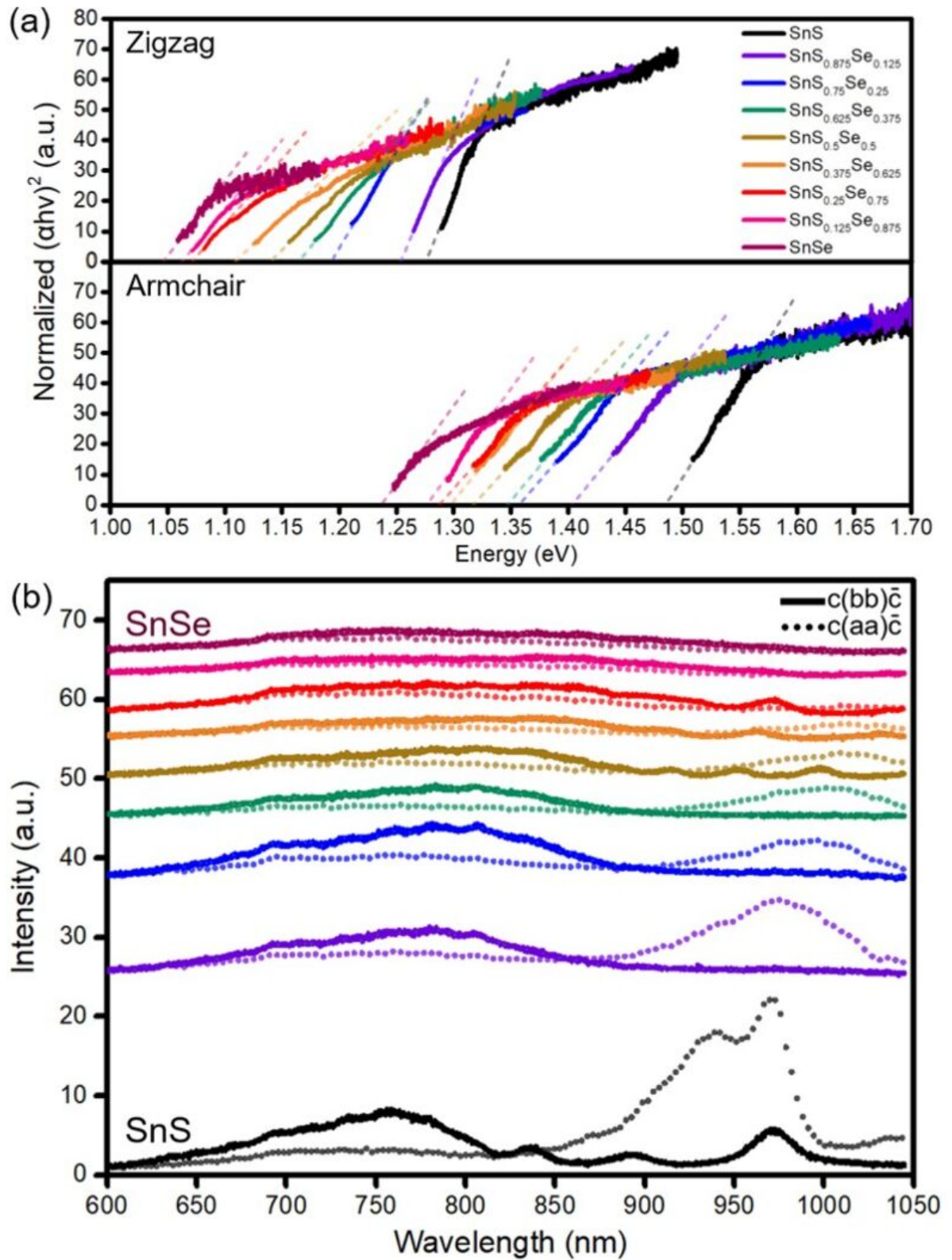


This is the author's peer reviewed, accepted manuscript. However, the online version of record will be different from this version once it has been copyedited and typeset.

PLEASE CITE THIS ARTICLE AS DOI: 10.1063/1.5128717



This is the author's peer reviewed, accepted manuscript. However, the online version of record will be different from this version once it has been copyedited and typeset.  
PLEASE CITE THIS ARTICLE AS DOI: 10.1063/1.5128717



This is the author's peer reviewed, accepted manuscript. However, the online version of record will be different from this version once it has been copyedited and typeset.  
PLEASE CITE THIS ARTICLE AS DOI: 10.1063/1.5128717

